Formation of C—S—H and M—S—H gels in alkali-activated materials based on marl by-products from phosphate mines

S. Mabroum [a,b], I. Garcia-Lodeiro [c], M.T. Blanco-Varela [c], Y. Taha [b], S. Chhaiba [c], S. Indris [d], M. Benzaazoua [b], M. Mansori [a], R. Hakkou [a,b,*]

[a] Cadi Ayyad University (UCA), Faculty of Science and Technology, IMED-Lab, BP549 Av. A. El Khattabi, Marrakech, Morocco
[b] Mohammed VI Polytechnic University (UM6P), Geology & Sustainable Mining Institute (GSMI), Lot 660, Hay Moulay Rachid, Benguerir, Morocco
[c] Eduardo Torroja Institute (IETcc-CSIC), Department of Materials, Madrid, Spain
[d] Institute for Applied Materials - Energy Storage Systems, Karlsruhe Institute of Technology (KIT), Hermann-von-Helmholtz Platz 1, Eggenstein-Leopoldshafen, Germany

ARTICLE INFO

Keywords:
Phosphate mine wastes
AAMs
Marls
Recycling
Calcination temperature
Geopolymers

ABSTRACT

Marls present high volume of phosphate waste rocks that are chemically inert, but their disposal creates diverse environmental issues. This study aims to evaluate the reuse of white marls from phosphate mines as a precursor to produce Alkali-Activated Materials (AAM). White marls containing palygorskite clay were calcined up to 850 °C. The alkali activation process involved the use of calcined marls (as a precursor) and NaOH:Na_2SiO_3 as activators. Marls features were identified by X-ray Diffraction, X-ray Fluorescence, Fourier-transform infrared spectroscopy and Thermo-gravimetric analysis. In addition, the dissolution of Al and Si species from the marl was studied for different Sodium hydroxide concentrations and calcination temperatures. Furthermore, the compressive strength of elaborated AAM was measured, and selected samples were characterized using several methods including Solid-state ^{29}Si – ^{27}Al Nuclear Magnetic Resonance spectroscopy and Scanning Electron Microscopy. The XRD and NMR results indicated the co-precipitation of C—S—H and M—S—H with the presence of low amount of C/N-(A)-S—H explained by the content of aluminum in marl. This result was confirmed by EDX and FTIR analysis. While the optimum compressive strength of 38 MPa was obtained for AAM based on calcined marl at 750 °C. This study results revealed that marls waste rocks could be used as a precursor for the formulation of AAM in construction applications.

1. Introduction

Alkali-activated materials (AMMs) are produced by mixing an aluminosilicate precursor, usually blast furnace slags (BFS) or coal fly ashes (FA), with an activator solution (mixture of sodium hydroxide and sodium silicate as the most effective activator), which is generally a strong alkaline medium [1,2]. The main binder phase in AAMs when the precursor is rich in calcium (such as the BFS) is a calcium aluminosilicate hydrate gel (C-A—S—H). AAMs are known to have interesting properties making their application beneficial in several engineering fields. These cementitious materials showed interesting properties in construction applications [3], stabilization/solidification technology [4] and mine backfill fabrication [5]. Alkali activation technology involves the use of diverse natural aluminosilicate sources as well as industrial wastes or by-products including mine wastes and tailings (MT) [6].

Recently, much attention has been paid to the mine wastes or tailings usage as an alternative way to develop a new approach in mine wastes management and to produce cementitious materials as an alternative to conventional construction materials (based in PC) [7,8]. The mining sector plays a vital role in sustaining social growth and developing global economies [9]. Nevertheless, the development of mineral production remains as one of the world's biggest wastes accumulators [10]. MT and waste rocks are the principal secondary materials produced

Abbreviations: AAMs, Alkali-Activated Materials; MT, Mine Tailings; XRD, X-Ray Diffraction; XRF, X-Ray Fluorescence; TGA, Thermo-gravimetric Analysis; FTIR, Fourier Transformed Infrared Spectroscopy; BET, Brunauer, Emmett and Teller; NMR, Nuclear Magnetic Resonance; SEM, Scanning Electron Microscopy; CM, Calcined Marl; RM, Raw Marl; C-S-H, Calcium Silicate Hydrate; M-S-H, Magnesium Silicate Hydrate; AAM650, AAM based on marl calcined at 650°C; AAM750, AAM based on marl calcined at 750°C; AAM850, AAM based on marl calcined at 850°C; UCS, Uniaxial Compressive Strength.

* Corresponding author at: Cadi Ayyad University (UCA), Faculty of Science and Technology, IMED-Lab, BP549 Av. A. El Khattabi, Marrakech, Morocco.
E-mail address: rachid.hakkou@um6p.ma (R. Hakkou).

during mining and processing operations [11,12]. Thus, these wastes are now considered as by-products that are deposited in dumps or stockpiles, depending on the type of waste, causing several environmental issues [13,14]. Generally, mine wastes are largely valorized in the construction field in several applications. Coal mine wastes and phosphate clays are recycled in manufacturing bricks [15,16]. El Machi et al. used phosphate wastes rocks as coarse aggregate in concrete formulations revealing important mechanical behavior [17,18]. Additionally, phosphate ore tailings were combined with polymeric wastes to produce lightweight aggregates [19]. Bahhou et al. have recycled of phosphate mine wastes as supplementary cementitious materials [20,21]. Magnesium-based cement has attracted much attention for its promising properties as a partial replacement for OPC [22]. Magnesium based cement systems have been investigated in different applications including the carbonation for strength gain and the formation of magnesium silicate hydrate (M—S—H) within MgO-SiO_2 blends [23,24]. Recent works on cementitious materials with the presence of reactive MgO have revealed that M—S—H could be formed by the reaction between an Mg-based source (MgO, $Mg(OH)_2$) and a silica source, resulting in a binder that can be used in certain applications such as building materials [25]. Within MgO-SiO_2-H_2O systems, M—S—H is produced via the reaction between Mg^{2+} and dissolved silica complexes [26]. The main factors influencing M—S—H formation are the chemical and physical properties of the precursors, mix and curing conditions and pH value. Ben Haha et al. showed that the presence of higher MgO content in blast furnace slags activated by using sodium silicate enhanced the compressive strength and reduced porosity [27]. The calcination of $MgCO_3$ at a temperature around 1000 °C produces reactive MgO that is responsible for the acceleration of the early-stage reaction, reducing the drying shrinkage, and improving the carbonation resistance [28]. Those important properties are produced due to the formation of C-M—S—H [26]. However, Lothenbach et al. have established that "M—C—S—H" phase could not be formed due to the presence of different silicate structures [29]. Nevertheless, according to their study, separate M—S—H and C—S—H phases could be produced in systems that contain both Mg^{2+} and Ca^{2+} sources [29]. In addition, some studies have proposed that magnesium could be incorporated in C—S—H, however no clear experimental statement was claimed [28];

In the case of AAMs, the dihydroxylation or calcination of some aluminosilicate precursors, specifically mine wastes, results in improving their reactivity to make them able to dissolve easily in alkaline mediums [30]. Furthermore, calcination is a promising pretreatment process to enhance the solubility of MT and promote their geopolymerization [31]. Several studies have proved that mine wastes present important properties as aluminosilicate precursors [32]. The alkaline roasting of vanadium tailings at T = 450 °C for 1 h destructs of crystalline structures allowing a better dissolution of Si and Al [33]. Moreover, calcination of red mud from bauxite ores at T = 800 °C for 1 h leads to the katoite dihydroxylation [34]. After fast cooling fired bauxite residue from T = 1100 °C, semi-vitreous phase was formed [35]. While montmorillonite clay contained in phosphates by-products was totally dehydroxylated at T = 900 °C. Furthermore, calcination of marls at T = 750 °C allows a compressive strength of 38 MPa at 120 days [36,37].

Calcination clays have shown important properties as precursors of AAM [38]. Metakaolin is the most widely clay used as a precursor in alkali-activated materials; this mineral is produced by the calcination of kaolin clays. Nevertheless, the high cost and scarcity of its reserves have resulted in the importance of involving the use of other clays, such as illite and smectite, and calcined marls [39]. Raw marl (RM) is constituted by a variety of clay minerals, carbonates and quartz in different proportions. The calcination of RM at an adequate temperature leads to the development of pozzolanic activity providing important mechanical strength [40]. The pozzolanic reactivity of RM corresponds to the formed glassy phase, which indicates the structural disorder induced by the calcination, in depends on the mineralogy of the contained clay [21]. Numerous works concluded that the highest pozzolanic reactivity of most marls is achieved at around 800 ∘C. This statement is explained by the nature of contained clays, which are usually montmorillonite, palygorskite, and illite.

The present study investigates the effect of calcination temperature of RM by-products from phosphate mines on the mechanical and microstructural behavior of elaborated AAM.

The main aim of this work is to valorize marl rocks from phosphate mines as precursors in the production of AAM. In addition, the objective of the study consists of investigating the properties of elaborated AAMs for construction application depending on the calcination temperature.

2. Materials and methods

2.1. Raw materials and geopolymers synthesis

In this study, RM are sampled directly from phosphate intercalation layers, are used as the only precursor for the formulation of alkali-activated materials. Sampling was carried out from the Gantour basin – Ben Guerir - phosphate mine site (OCP-SA, Morocco). Raw marl is mainly composed of SiO_2 present in quartz and tridymite. While it contains amounts of CaO and MgO indicating the presence of dolomite and fluorapatite. In addition, Palygorskite phase is present as a clayey mineral. Table 1 presents the chemical and physical characteristics of RM samples. RM rocks are crushed, ground, and sieved under 100 μm. After the mechanical preparation, the RM powder was calcined at different temperatures (650, 750 and 850 °C) to study the impact of calcination temperature on the properties of the MAA. The calcination was performed for 2 h with a heating of 10 °C /min. The selection of calcination temperature and rate depends on previous studies and TGA results [36,37].

For the formulation, the CM powder was blended with an activator solution made by mixing NaOH (10 M) and water glass (SiO_2/Na_2O = 3.2), at a water glass/NaOH ratio of 1 in weight. The liquid to solid ratio of the mixture is 1. The paste was stirred using mechanical agitator for 7 min and then introduced in cylindrical molds (O: 20 mm, H: 40 mm) sealed by plastic film. The curing regime was at T = 22 °C for t = 24 h before demolding. The UCS was evaluated at 7, 14, 28, and 120 days. Samples were stored in humid chamber at ambient temperature and 98 % humidity before being characterized. The characterization of elaborated geopolymers was performed at 120 days to obtain relatively long-term data.

2.2. Analysis methodology

Epsilon 4 Model - Malvern Panalytical and Bruker-AXS D8 powder diffractometer were used to define the chemical and mineralogical characteristics of RM. The XRD equipment was operating by Cu Kα radiation (λ = 0.154186 nm) from 2θ of 2° to 70°. Software DiffracPlus EVA and TOPAS associated to a chemical reconciliation were used to identify and quantify the existing phases. Nicolet 5700 spectrometer was employed to perform the FTIR analysis between 400 cm^{-1} and 4000 cm^{-1} at 4 cm^{-1} resolution using powdered samples embedded in KBr pellets (0,001 g sample/0,099 g KBr). TG analysis was performed under air (30 ml/min) at 900 °C with 10 °C/min speed using 35 mg of sample. Moreover, TESCANVEGA3-SEM was used to investigate the microstructure. Laser particle size analyzer, Mastersizer 2000 and Micromeritic Gemini VII Equipments were used to measure the size distribution and surface area, respectively. In addition, helium Pycnometer (AccuPyc II 1340) equipment was employed to determine the density. The UCS was measured by a uniaxial hydraulic press using the Instron 3369 Universal Testing Machine with a load capacity of 30 kN.

Magic-angle spinning (MAS) nuclear magnetic resonance (NMR) spectroscopy was carried out on a Bruker Advance 500 MHz spectrometer at a magnetic field of 11.7 T, which corresponds to resonance frequencies of 130.3 MHz (^{27}Al) and 99.4 MHz (^{29}Si). Spectra were acquired with a Hahn-echo pulse sequence for ^{27}Al, and with a single-

Table 1
Mineralogical, chemical, and physical characteristics of RM.

Chemical Composition, wt. %	LOI	SiO_2	Al_2O_3	CaO	MgO	F_2O_3	P_2O_5	K_2O	TiO_2
	24.00	46.00	1.05	14.60	12.50	0.84	0.72	0.24	0.07
Physical properties	D_{50} (μm)	D_{90} (μm)		Specific surface (m^2/g)			Density (g/cm^3)		
	22.12	79.23		83.25			2.12		
Mineralogical composition, wt. %	Tridymite SiO_2	Dolomite CaMg $(CO_3)_2$	Palygorskite $(Mg,Al)_2Si_4O_{10}(OH)\bullet4(H_2O)$		Hematite Fe_2O_3		Fluorapatite $Ca_5(PO_4)_3F$		Quartz SiO_2
	19.4	43.9	17		1		1.70		17

LOI: loss of ignition at 1050 °C.

pulse sequence for ^{29}Si. The recycle delay was 5 s and the π/s pulse length was about 2 μs. The spectra were referenced to 1 M $Al(NO_3)_3$ for ^{27}Al, and tetramethyl silane for ^{29}Si.

2.3. Si and Al dissolution tests

Dissolution test was carried out in order to study the leaching of both Si and Al for different temperatures and to choose the adequate NaOH concentration. The amount of dissolved Al and Si species from RM was defined by the leaching method under different alkaline concentrations at different calcination temperatures (T1 = 650 °C, T2 = 750 °C, and T3 = 850 °C). The test was conducted by stirring 0.5 g of CM with 50 ml of NaOH for concentrations of 8, 10, and 12 M at a speed of 120 rpm for 4 h. High concentrations of NaOH were used to further investigate the variation in the Si and Al dissolution degree of the tested powders. The dissolution conditions were defined based on previous studies [31,41]. Extended periods of time make the solutions very viscous. After mixing, the centrifugation was executed for 10 min at 6000 rpm, then the filtration using a vacuum pump. The filtrates were collected for testing silicon and aluminum ion dissolution by ICP-AES.

3. Results and discussion

3.1. Characterization of the precursor

XRD patterns of raw marl (RM) and calcined marl (CM) are presented in Fig. 1. The RM shows a high percentage of dolomite phase (CaMg $(CO_3)_2$), quartz (SiO_2), and Tridymite (SiO_2), while fluorapatite ($Ca_5(PO_4)_3F$) is present in low amount. Palygorskite ((Mg, $Al)_2Si_4O_{10}(OH)$-4(H_2O)) is observed at 2 θ values of 8.85°, 13.95°, and 16.46°. With rising the temperature, the peak at 8.85° shifted to 9.05°, resulting from the elimination of water from the interfoliate space [42]. This fact could be explained by the variation of the water content, resulting in a change in the position of the peaks [43]. At 650 °C, the intensity of palygorskite peaks decreased until disappearing at 850 °C indicating the complete dihydroxylation reaction [44]. Furthermore, the decarbonation of dolomite took place resulting in the decrease of intensity peaks and the formation of gehlenite and enstatite ($MgSiO_3$) phases [36,45]. However, from 750 °C dolomite disappeared totally indicating the full decarbonation and leading to the formation of periclase (MgO) [38]. Previous studies have showed that the complete decomposition of dolomite is commonly reported between 700 °C and 800 °C [48]. In addition, portlandite phase ($Ca(OH)_2$) is detected after calcining at 750 °C, while with increasing the temperature, lime (CaO) was identified. The presence of portlandite, regardless the calcilination temperature used can be explained as follow: the sample interact with water of the atmosphere leading to the hydration of CaO, then the formation of portlandite following the reaction (3) [49]. The phenomenon that occurred during the calcination could be explained by equations (1)–(3).

$$CaMg(CO_3)_2 \rightarrow CaCO_3 + MgO + CO_2\ (700\ ^\circ C) \quad (1)$$

$$CaCO_3 \rightarrow CaO + CO_2\ (850\ ^\circ C) \quad (2)$$

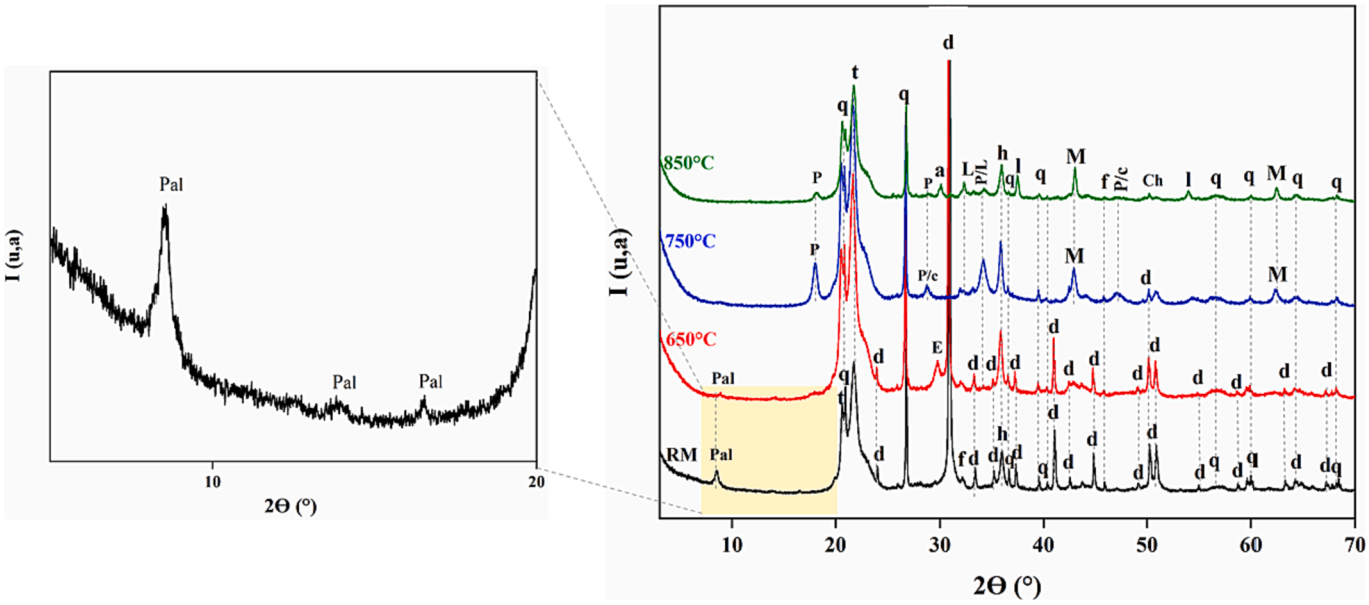

Fig. 1. XRD patterns of RM and CM at 650 °C, 750 °C and 850 °C. Pal: palygorskite (COD9005565), q: quartz (COD9012600), d: dolomite (COD9004931), t: tridymite (COD9005269), f: fluorapatite (COD9009978), P: portlandite (COD1001769), E: enstatite (COD9014117), c: calcite (COD9015066), l: lime (COD1011327), L: larnite (COD9012791), M: periclase (COD9006747), a: augite (COD1200006), and h: hematite.

Table 2
Existing phases in RM and CM at 650, 750, and 850 °C.

Raw marl	CM at different temperatures		
	T1 = 650 °C	T2 = 750 °C	T3 = 850 °C
Quartz	Quartz	Quartz	Quartz
Palygorskite	Palygorskite	Tridymite	Tridymite
Tridymite	Tridymite	Calcite	Calcite
Dolomite	Dolomite	Portlandite	Portlandite
Fluorapatite	Fluorapatite	Fluorapatite	Fluorapatite
Hematite	Hematite	Hematite	Hematite
	Enstatite	Periclase	Periclase
			Lime
			Larnite
			Augite

$$CaO + H_2O\ (air) \rightarrow Ca(OH)_2\ (ambient\ T) \quad (3)$$

In addition, at 850 °C larnite (Ca_2SiO_4) was identified and formed by the reaction between CaO from the decomposition of dolomite and silicon oxides from the palygorskite [44]. The formation of Larnite (C_2S) phase is confirmed by Poussardin et al. [42]. They stated that calcining marlstone that contain palygorskite clay at 800 °C leads to the formation of C_2S phase. Traces of calcite ($CaCO_3$) were detected at 850 °C. However, the temperature did not influence fluorapatite, quartz, and tridymite. Augite phase ($(Ca,Na)(Mg,Fe,Al,Ti)(Si,Al)_2O_6$) is detected after calcining at 850 °C, this crystalline phase is a product of recrystallization reaction [42]. Table 2 summarizes the phases contained in raw and calcined marl at different temperatures.

FTIR spectra of RM and CM are shown in Fig. 2. In all spectra, bands of stretching and bending vibrations of H—O—H bonds of water molecules are respectively located at 3440 and 1658 cm ^{1}. The intensity of these bands decreased after calcination but still appeared at 850 °C. This could be explained by the fact that KBr is highly hygroscopic. The bands located around 3640 cm-1are attributed to asymmetric stretching vibrations of O—H bonds in portlandite indicating that the sample was hydrated after calcination explaining the presence of portlandite in XRD spectra [13]. C═O stretching vibration band is located at 1440 cm ^{1}, which is present in dolomite phase, that decreased with calcining marls resulting from the decomposition of carbonates [50]. However, this band still appeared at 850 °C but with much lower intensity corresponding to the presence of calcite traces as mentioned in XRD. The bands at 727 cm ^{1} and 879 cm ^{1} are characteristic of the presence of dolomite that disappeared after calcination at 850 °C. These bands intensity decreased with the increase of temperature until disappearing at 850 °C. Three bands at 1100 cm ^{1}, 1038 cm ^{1} and 989 cm ^{1} are associated with Si-O-Si (Si-bridging oxygen-Si) bonds vibrations present in palygorskite [51]. The band at 478 cm-1 is attributed to bending vibration of Si–O. The presence of quartz is confirmed by a band at 793 cm ^{1,} which corresponds to Si-O-Si stretching vibration [37]. A peak-like shoulder at 908 cm ^{1} appeared in RM, and its intensity decreased with calcining. This peak is attributed to Al–OH–Al deformation and the disappearance of this band confirmed the dihydroxylation of clay [52]. The changes showed in FTIR results are in accordance with the XRD ones, confirming that the changes in the clay structure due to the calcination correspond to the loss of different types of water molecules in the clayey mineral.

The thermal behavior of raw marl was presented by thermogravimetric curves in Fig. 3. No peak was detected around 120 °C due to the drying of the sample before the analysis. However, the curve showed three different mass losses. At 350 °C, the first mass loss indicates the start of palygorskite dihydroxylation. While the second loss is presented by a peak around T = 600 °C which could be assigned to the structural collapse of palygorskite. In addition, the last large weight loss around 776 °C is assigned to the decomposition of dolomite [53].

3.2. *^{29}Si and ^{27}Al MAS NMR of calcined marls at different temperatures*

The ^{27}Al MAS NMR spectra of calcined marls at different temperatures are shown in Fig. 4.A. The curves display-two main peaks at + 14 and + 55 ppm. The first resonance is attributed to 6-coordinated aluminum corresponding to the aluminum present in the palygorskite [54]. The second resonance at + 54 ppm corresponds to 4-coordinated aluminum related due to the transformation of Al(VI) to Al(IV) consequence of the dihydroxylation process of palygorskite [42]. The peak

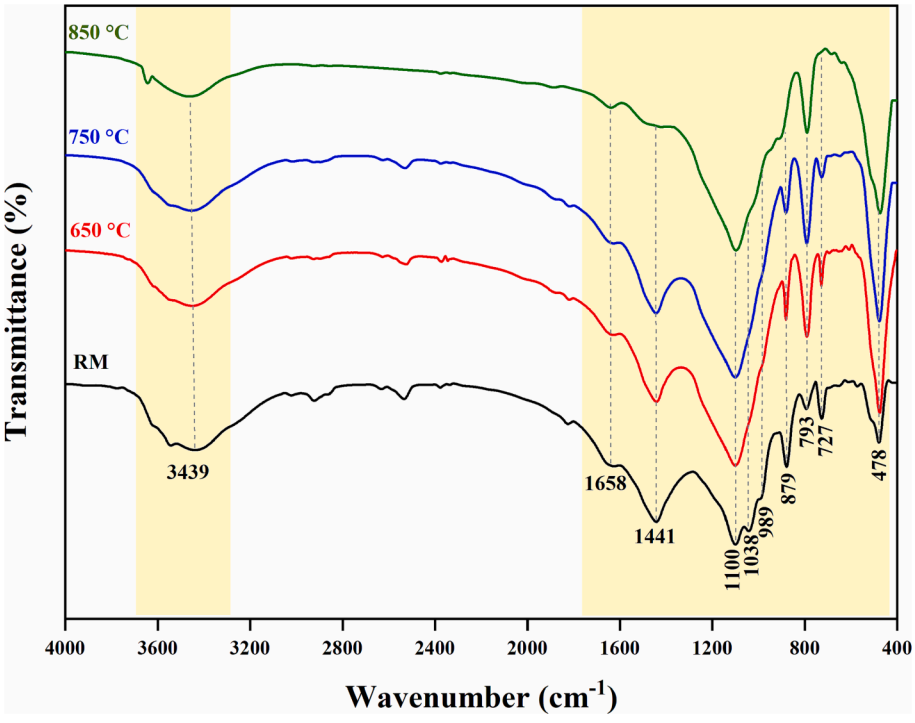

Fig. 2. FTIR curves of RM and CM after calcination at 650, 750, and 850 °C.

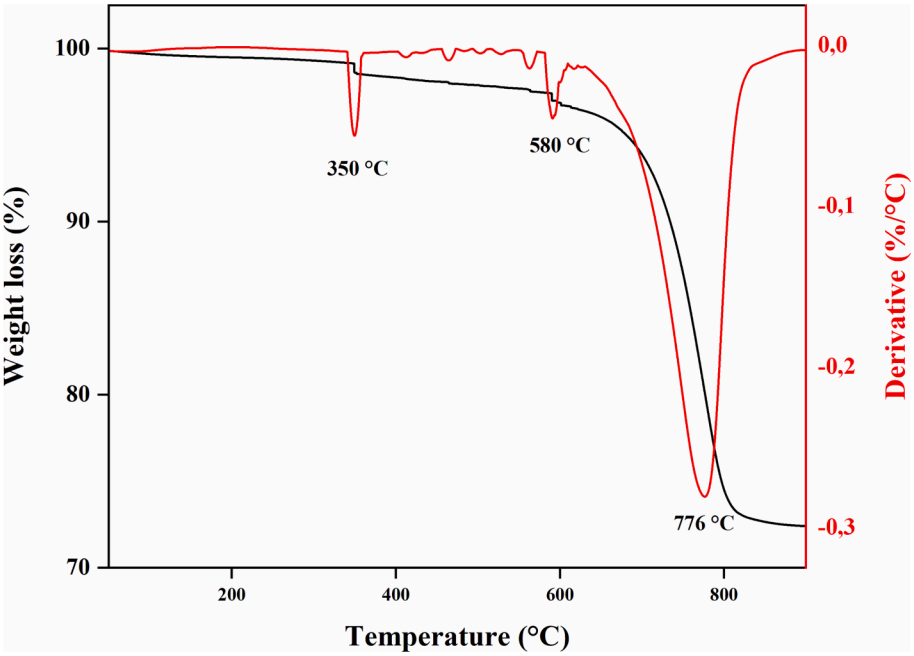

Fig. 3. TGA-DTG curves of RM.

corresponding to Al(VI) decreased slightly with increasing the temperature from 79 % to 77.3 % for 650 °C and 750 °C, respectively. This fact could be explained by the dihydroxylation of the palygorskite phase. However, Al(VI) still appeared at all temperatures due to the incomplete decomposition of palygorskite and the formation of new phases resulting from the recrystallization of the sample. Fig. 4.B displays the evolution of the ^{29}Si MAS- NMR spectra of the calcined marls at different temperatures. The resonance at 83 ppm is attributed to Q^2 sites in enstatite [55]. Resonance at 89 ppm corresponds to Q^2 in palygorskite. In addition, peaks located at 96 ppm and 99 ppm are attributed to Q^3(mAl) existing in palygorskite [42,56]. The intensity of these sites decreased with increasing the temperature to 850 °C indicating the dehydration of palygorskite. The spectra of calcined marls at different temperatures exhibited a wide signal centered at – 113 ppm, assigned to the Q^4 units in the amorphous silica tridymite [57]. A resonance around 72 ppm appeared at the spectrum of marls calcined at 850 °C and could be assigned to Q^0 sites existing in larnite that is formed at this temperature according to XRD results.

3.3. *Si and Al leaching test*

The results of the measurement of Si and Al leached from CM at various temperatures in an alkaline medium with different concentrations are shown in Fig. 5. The maximum Si concentration of about 990

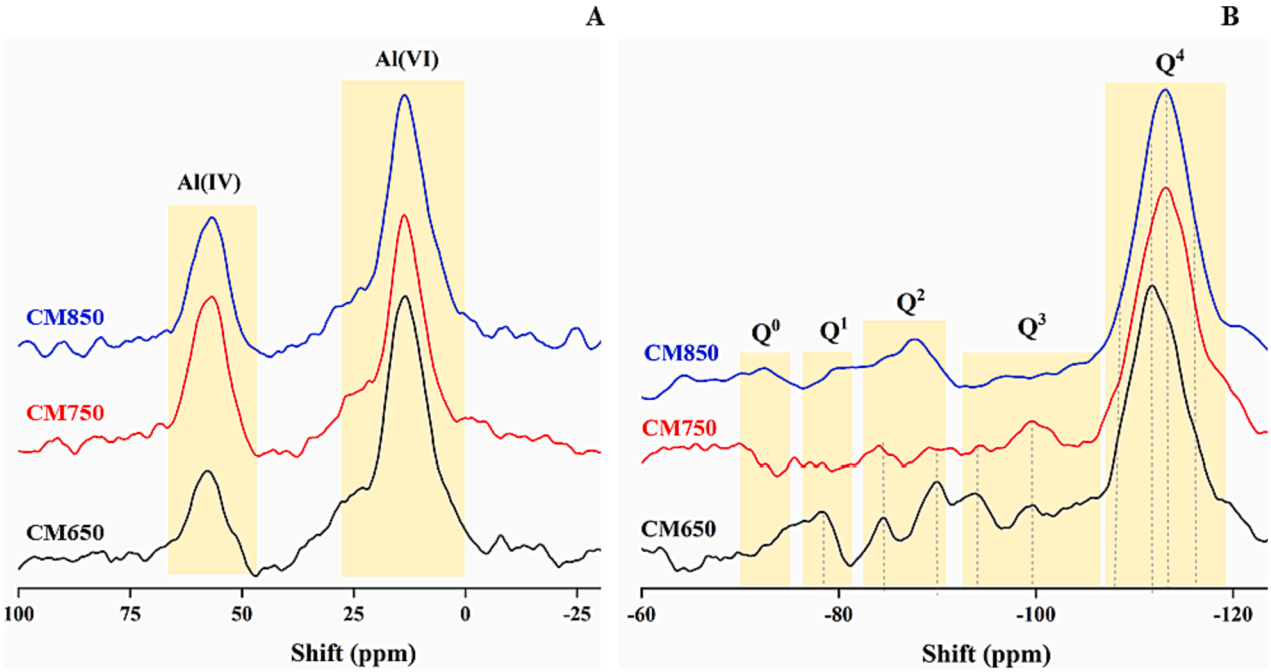

Fig. 4. **A**: ^{27}Al MAS NMR spectra of AAM, **B:** ^{29}Si MAS NMR spectra of elaborated AAM,

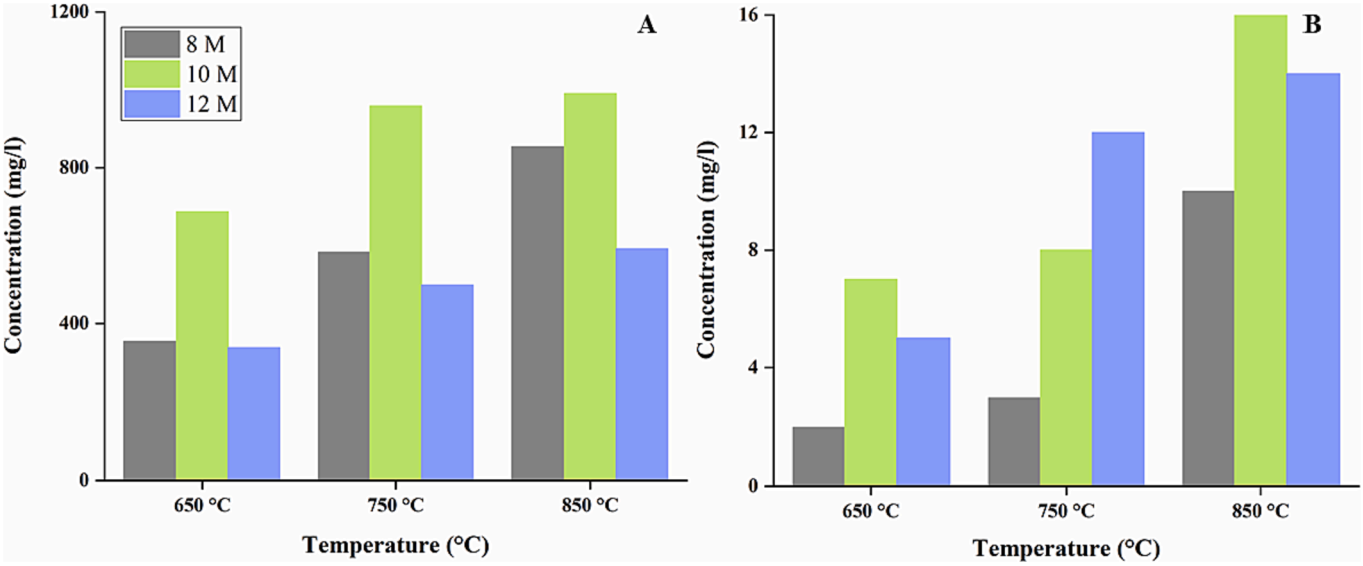

Fig. 5. **A.** Si concentration (ppm), **B.** Al concentration (ppm), for 8, 10, and 12 M NaOH at 650, 750, and 850 °C.

mg/l was obtained with 10 M NaOH for a powder calcined at 850 °C. At the same temperature, for 8 M and 12 M NaOH, the concentrations were much smaller at 766 and 592 mg/l, respectively. At 8 M NaOH concentration, the dissolution reaction of Si was slow resulting from low alkalinity comparing to 10 M and 12 M. For the 12 M NaOH, the dissolution is decreased due to the increase in coagulation of silica [58]. However, for the same NaOH concentration, the solubility of silica increases with increasing the temperature of calcination. As it was expected, the concentration of Al ions was considerably lower than that of Si ions, as shown in Fig. 5B. This could be explained by the low content of Al in the raw marl. For 8 M NaOH, the amount of leached Al was smaller for all samples calcined at different temperatures. The Al concentration increases from 10 mg/l to 16 mg/l for NaOH 10 M with temperature going from T1 = 650 °C to T2 = 850 °C. While for 12 M the concentration decreased to reach 14 mg/l for 850 °C. This reduction could be assigned to the recrystallisation of the powder calcined at 850 °C. Thus, the leaching of Si and Al necessitate longer time and/or a higher temperature [59]. Rattanasak et al. have mentioned that the subsequent formation of precipitates and gels leads to the depletion of ions and thickening the solution which resulted in retarded leaching of ions [58]. In addition, Ouffa et al, studied the dissolution of fifteen pure aluminosilicate minerals in alkaline medium was investigated [31]. Their results revealed that the dissolution depends mainly on the crystallization conditions of the minerals as well as their chemical composition. The results of leaching tests show that the powder calcined at T3 = 850 °C reaches the maximum concentration of Si and Al. In addition, the use of 10 M NaOH was adequate for the synthesis of AAM.

3.4. Mechanical strengths of AAMs

Fig. 6 illustrates the UCS of AAM650, AAM750, and AAM850 after 7, 14, 28, and 120 days. As shown in this Figure, the UCS values increased with the age. The increase was slight between 7 and 14 days to reach approximatively 2 MPa for AAM650 and AAM850, while it attained 2.8 MPa for GP750. At this age, the difference of UCS for all sample was not large. This fact could be described by the very slow dissolution rate of alumina and silica. This phenomenon is generally occurring for low temperature curing [60]. After 28 days of curing, AAM750 indicated a UCS of about 7.5 MPa. The highest strength of 38 MPa was recorded after 120 days for the same geopolymer, performed by using marls calcined at 750 °C, while it did not exceed 20 MPa and 26 MPa for AAM650 and AAM850, respectively. In addition, the high compressive strength obtained for AAM750 could be explained by the presence of C_2S in the powder calcined at this temperature as Sanchez et al (2016) stated that the C_2S phase possesses a positive effect on the mechanical strength in alkali-activated materials [61]. In addition, the hydration of C_2S, produces C—S—H which should contribute to the mechanical strengths. Also, the presence of CaO in the calcined powder affects positively the strength, according to Temunjim (2009) the compressive strength of alkali-activated materials was important due to the formation of amorphous C—S—H gel leading to the decrease of porosity [62]. For AAM650, the development of compressive strength is limited by the fact that at 650 °C the palygorskite clay was not totally dehydroxylated hindering the dissolution of silica and alumina.

The decrease of mechanical strength for AAM850 could be explained by the recrystallisation of the calcined powder. It is known in the literature that calcining at temperatures higher than 800 °C leads to the recrystallization responsible for reducing the compressive strength [63]. In general, new crystalline phases such as mullite and spinel are formed when calcining at elevated temperatures [64].

3.5. Characterization of elaborated AAMs

XRD patterns of geopolymers based on calcined marl are presented in Fig. 7. The characterization of AAMs was performed at 120 curing days. The remaining phases after the alkali-activation reaction were quartz (SiO_2), fluorapatite ($Ca_5(PO_4)_3F$), and enstatite ($MgSiO_3$). These phases are still present and not affected in alkaline medium [37,65]. While tridymite (SiO_2), augite ($(Ca,Na)(Mg,Fe,Al,Ti)(Si,Al)_2O_6$), larnite ($Ca_2SiO_4$), portlandite ($Ca(OH)_2$) and lime (CaO) phases were totally disappeared at all temperatures. However, dolomite ($CaMg(CO_3)_2$) and palygorskite ($(Mg_2Al_2)Si_8O_{20}(OH)_2{\cdot}4H_2O$), present in the raw material, were also present in AMMs made of powder calcined at 650 °C, which did not completely decompose at this temperature.

A broad diffuse hump appeared in the angular range between 20° and 35° and indicates the presence of amorphous phase [36]. Considering the chemical composition of the precursor, this amorphous phase could refer to a C—S—H type gel, as the soluble silicate reacts with Ca from larnite and portlandite promoting the formation of C—S—H [65,66]. The intensity of periclase (MgO) decreased consequently after alkali-activation for AAM650 and AAM750. According to the literature, the reactive Mg reacts with Si–O to form M—S—H (magnesium silicate hydrate gel) [67]. This statement is in accordance with early works confirming that Mg is rapidly consumed to produce M—S—H when

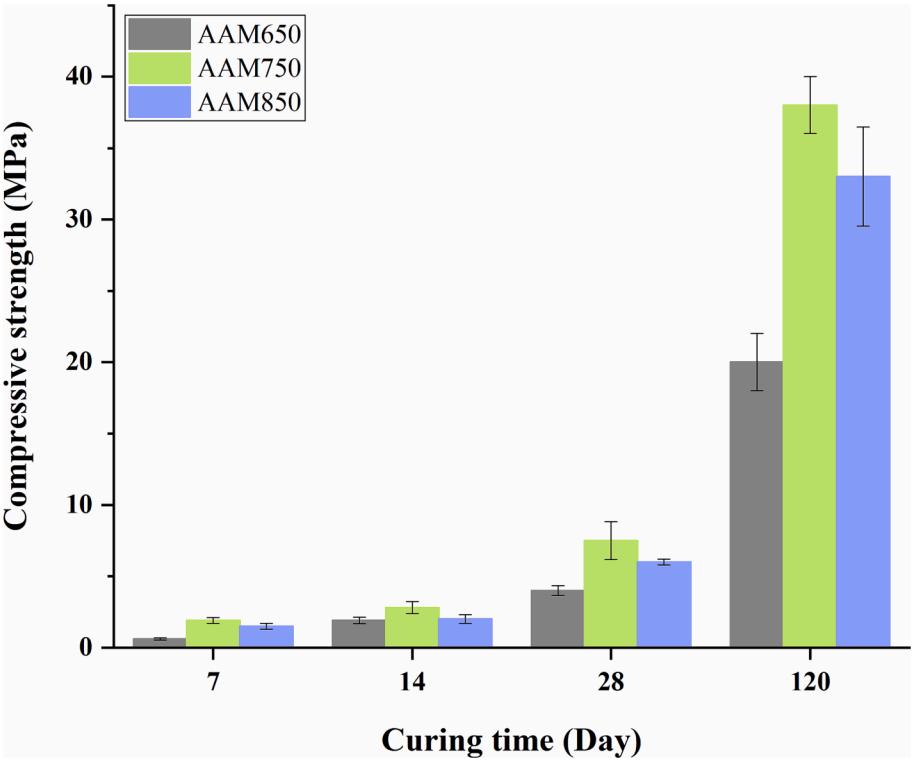

Fig. 6. UCS of AAMs after 7, 14, 28, and 120 curing days.

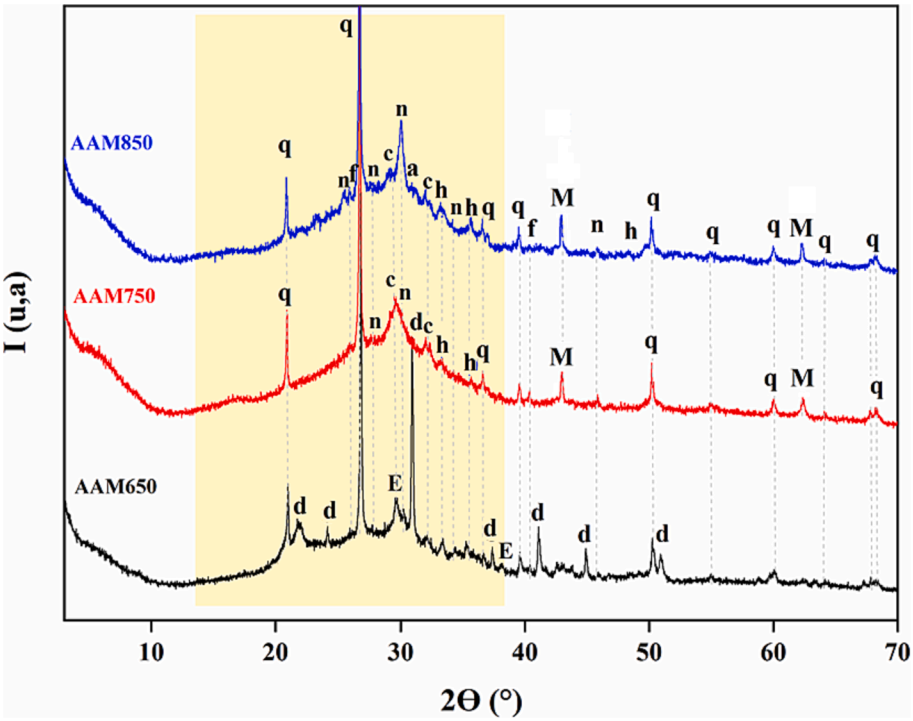

Fig. 7. XRD pattern of AAMs after 120 curing days. q: quartz (COD9012600), c: calcite (COD9015066), E: enstatite (COD9014117), M: periclase (COD9006747), d: dolomite (COD9004931), f: fluorapatite (COD9009978), h: hematite and n: natrite (COD9009418).

activating with slag [26]. Due to its poor crystallinity, M—S—H is difficult to be seen in XRD but could be formed confirming the existing hump [68]. Considering that the main products of AAMs, are usually *N*-A—S—H and/or C-A—S—H gel, the amorphous hump could be associated with one (or a mixture) of them. However, considering the lor proportion of Al, and considering the chemical composition, it seems much more probable the formation of a C—S—H or M—S—H gel. The XRD pattern of AAM750 showed the presence of calcite that resulted from the decomposition of dolomite after calcination. In addition, for all temperatures, reflections of natrite (Na_2CO_3) phase were detected. This

formation could be assigned to the excess of sodium, coming from the activator, which reacted with CO_2 in the air as stated by Rakhimova et al. and Mabroum et al. [36,40].

FTIR spectra of elaborated AAM are illustrated in Fig. 8. AAM synthesized using CM at different temperatures present the same bands, but the intensities differ. The broadband located between 2200 cm ^{1} and 3700 cm ^{1} in all spectra is assigned to O—H stretching vibration of water [69,70]. The little band at 3638 cm ^{1} could be attributed to the presence of amorphous portlandite, as this phase did not appear in XRD results. The band at 1653 cm ^{1} corresponds to the O—H bending of the water molecule [71]. In addition, carbonates (CO_3^{2-}) are presented by the band located at 1464 cm ^{1} confirming the presence of carbonates showed in XRD results [72]. The absorption band at 452 cm ^{1} and 798 cm ^{1} corresponds to Si–O bending and Si-O-Si stretching vibrations, respectively [73]. These bands are characteristic of the presence of quartz. Furthermore, bands at 895 cm ^{1} in AAM650 could be attributed to (CO_3^{2-}) specially dolomite. This band disappeared in AAM750 and AAM850 as dolomite decomposed at these temperatures. While the band at 712 cm ^{1} appeared more intense in AAM650 and is attributed to the calcite. In addition, the band at 1047 cm ^{1} are typical of M—S—H [74]. A band like a shoulder is located at 974 cm ^{1} and could be assigned to C—S—H gel [29].

The TG and DTG curves of alkali-activated materials are shown in Fig. 9. The first weight loss is located in the range between 50 °C and 200 °C observed for all AAMs and corresponds to the loss of bound water adsorbed on the surface of C—S—H and M—S—H [75]. This loss could be associated with adorbed water or water from gels. The second loss is the same in all AAMs and is ranged between 200 °C and 450 °C. This loss corresponds to the dehydroxylation of bridged hydroxyl groups in C—S—H and M—S—H gel [75,76]. The third weight loss around 550 °C is related to the dehydroxylation of magnesium hydroxyl groups (Mg-OH) in M—S—H [77]. Losses ranging from 600 °C to 800 °C correspond to the decomposition of carbonates [78]. The results confirmed the results of XRD and FTIR.

3.6. ^{27}Al and ^{29}Si MAS NMR results

The ^{27}Al- NMR spectra of elaborated AAM are presented in Fig. 10.A. All spectra are dominated by a strong peak around + 13 ppm representing octahedral [AlO_6] units [79]. The Al(VI) in AAM650 and AAM750 is present in palygorskite which still appeared at these temperatures due to the incomplete dihydroxylation. This peak decreased from 80 % to 63 % with increasing the temperature from 650 °C to 750 °C, then increased to 71 % for 850 °C. In addition, it could be attributed to the recrystallization and subsequent forming of the Augite phase after the calcination at 850 °C. Furthermore, this broad Al(VI) resonance could be also attributed to M-(A)-S—H gel, as suggested by Bernard et al, proposing the possible substitution of Mg by Na or Ca in the formed N-(A)-S—H or C-(A)-S—H gels [80].

The second peak is observed in the range between + 55 and + 58 ppm and corresponds to tetrahedral Al(IV) units. The percentage of Al (IV) was at the maximum of 37 % for AAM750. Some additional intensity is found in the range between + 40 to + 30 ppm. This could be attributed to Al(V) units. This intensity is higher for the sample heated to 650 °C and starts to decrease with increasing the temperature of heating. It should be noticed that the global intensity of the peaks in the ^{27}Al NMR spectra is low due to the low amount of Al in these samples.

As shown in Fig. 10.B. The spectra of calcined marls at different temperatures exhibited a wide signal centered at – 113 ppm, assigned to the Q^4 units in the amorphous silica tridymite [64]. The intensity of these resonances declines significantly after the alkali-activation reaction, while new signals appear as the result of the formation of new alkaline reaction products. Comparing the ^{29}Si results of AAM to those of CM, resonances attributed to palygorskite (Q^2 and Q^3) are still appearing in AAM650 as this clay is not totally dehydroxylated in CM650. In addition, the resonances corresponding to quartz did not disappear for all AAM.

The local structures around Si have been investigated with ^{29}Si NMR in Fig. 11. It is clearly observed that all AAMs samples presented the

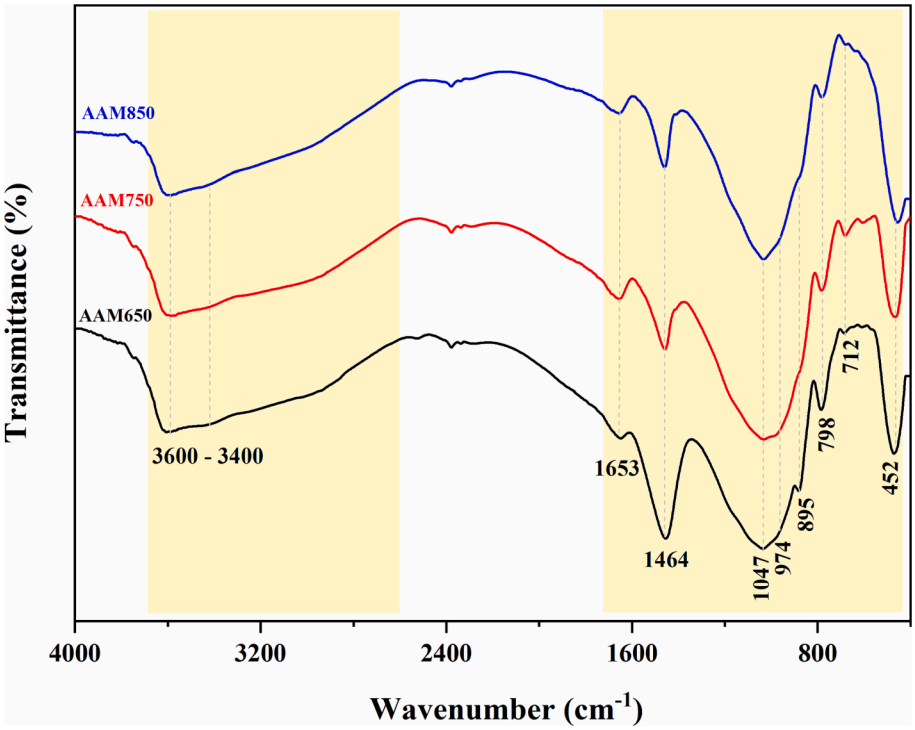

Fig. 8. FTIR curve of hardened material after 120 curing days.

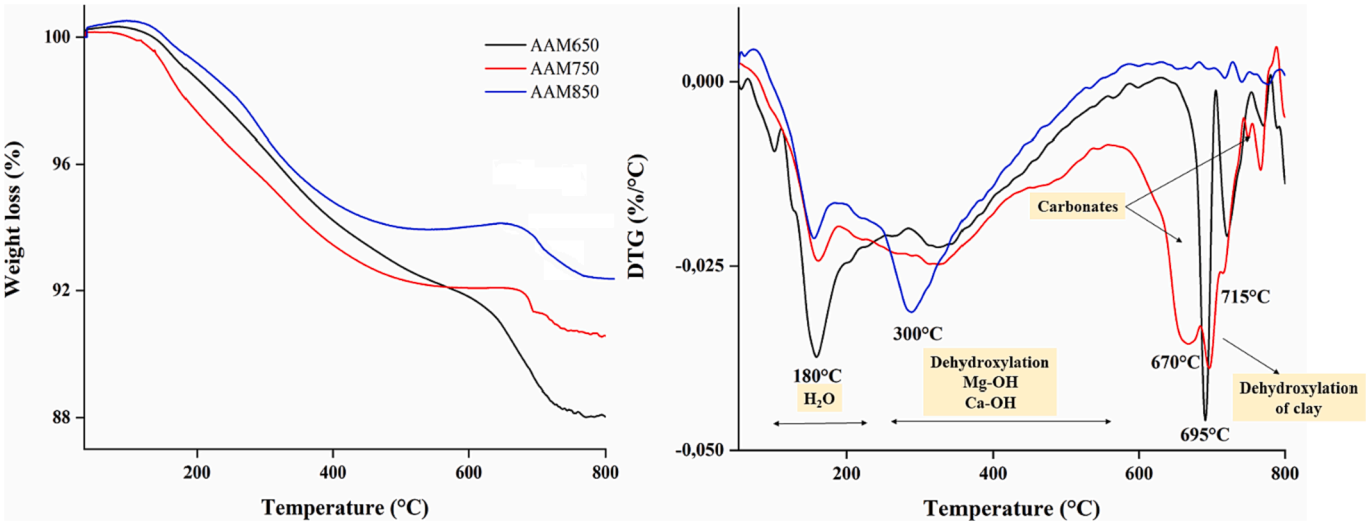

Fig. 9. TG and DTG of AAM650, AAM750 and AAM850.

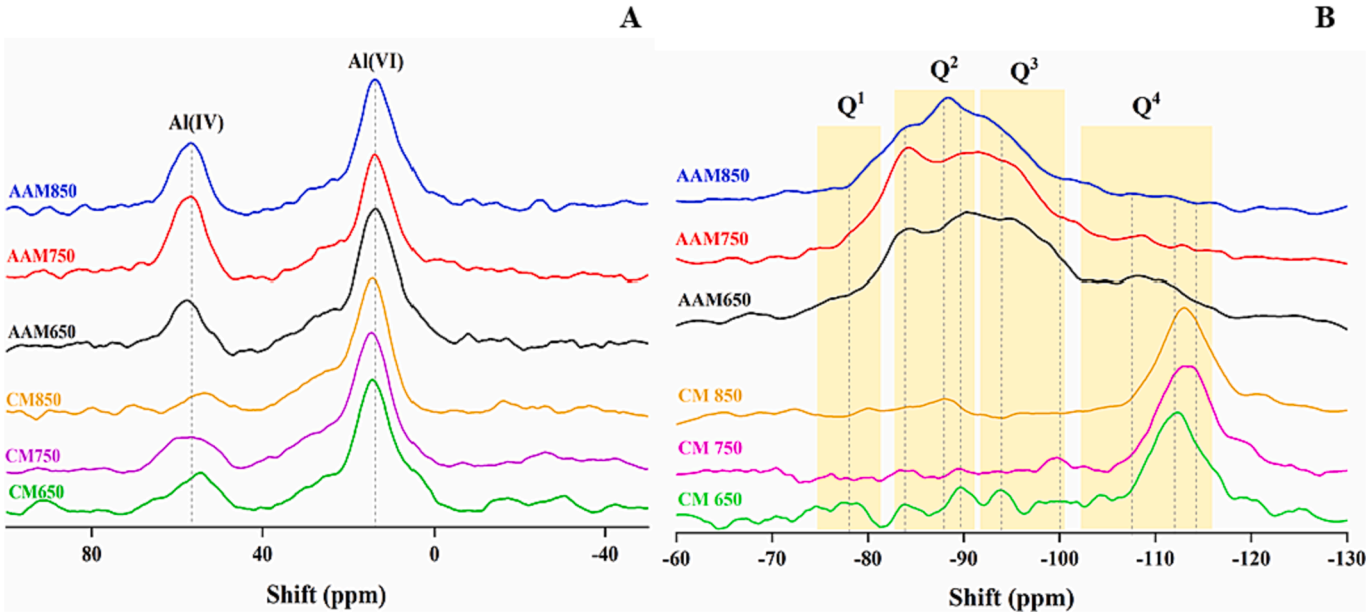

Fig. 10. **A:** ^{27}Al MAS NMR spectra of elaborated AAMs; the two peaks represent 6-coordinated Al (octahedral, Al(VI)) and 4-coordinated Al (tetrahedral, Al(IV)), **B:** ^{29}Si MAS NMR of calcined marls and elaborated AAMs.

same bands but with different intensities and a little shift due to the heat treatment of marl at different temperatures. In the literature, M—S—H gel is reported to have the silicon sites in coordination 1, 2, 3 and 4. (Q^4 (~100 ppm), Q^3 (~-92, 96 ppm), Q^2 (~- 85 ppm), and Q^1 (~-78 ppm)) [81]. However, the C—S—H gel shows structures of the layers, and the branching sites Q^3 (~-93 ppm), the chain middle groups Q^2 (~-85 pm), and the end groups Q^1 (~-79 ppm) [75]. The deconvoluted spectra of elaborated AAMs show the presence of several type of peaks. The resonances at 79 ppm, 83 ppm and 86 ppm correspond to the presence of Q^1, Q^2(1Al) and Q^2 sites in C—S—H gel, respectively [36,56]. According to Bernal et al. 2013, the peak at 82 ppm could be assigned to Q^2(1Al), characteristic of bridging tetrahedra sites of Si in which the Al is involved, or simply assigned to Q^2(L) existing in C—S—H [82]. Resonances at 88 ppm corresponds to Q^3(1Al) [83].

Resonance at 78 ppm is attributed to Q^1 in M—S—H gel, while those around 92 ppm, 94 ppm and 96 ppm could be attributed to Q^3 present in M—S—H as stated by Bernard *et al.* [77,78]. Q^4 sites are present at 98 ppm, 100 ppm and 108 ppm corresponding to Q^4(2Al), Q^4(1Al) and Q^4(0Al), respectively. The presence of these peaks could indicate the presence of hybrid (C,N)-A—S—H with very low content of Al or could correspond to silicon bridge gel existing in sodium silicate [75]. The hypothesis is, considering the time, usually (C,N)-A—S—H gel evolves to a C-A—S—H gel.

The resonances at 108 ppm and 112 ppm are attributed to Q^4 sites existing in quartz [84]. These results proved the coexistence of several gels including C—S—H, M—S—H, with the presence of little amount of (C,N)-A—S—H gels. The existence of these gels could explain the presence of the broad halo in the XRD spectra. On the other hand, the amount of formed (C,N)-A—S—H is approximatively the same around 12 % for all elaborated alkali-activated materials. While the formed M—S—H gel was higher in AAM750 of 33 % comparing with AAM650 that contains only 24 % and AAM850 with 27 % as seen in Table 3. These

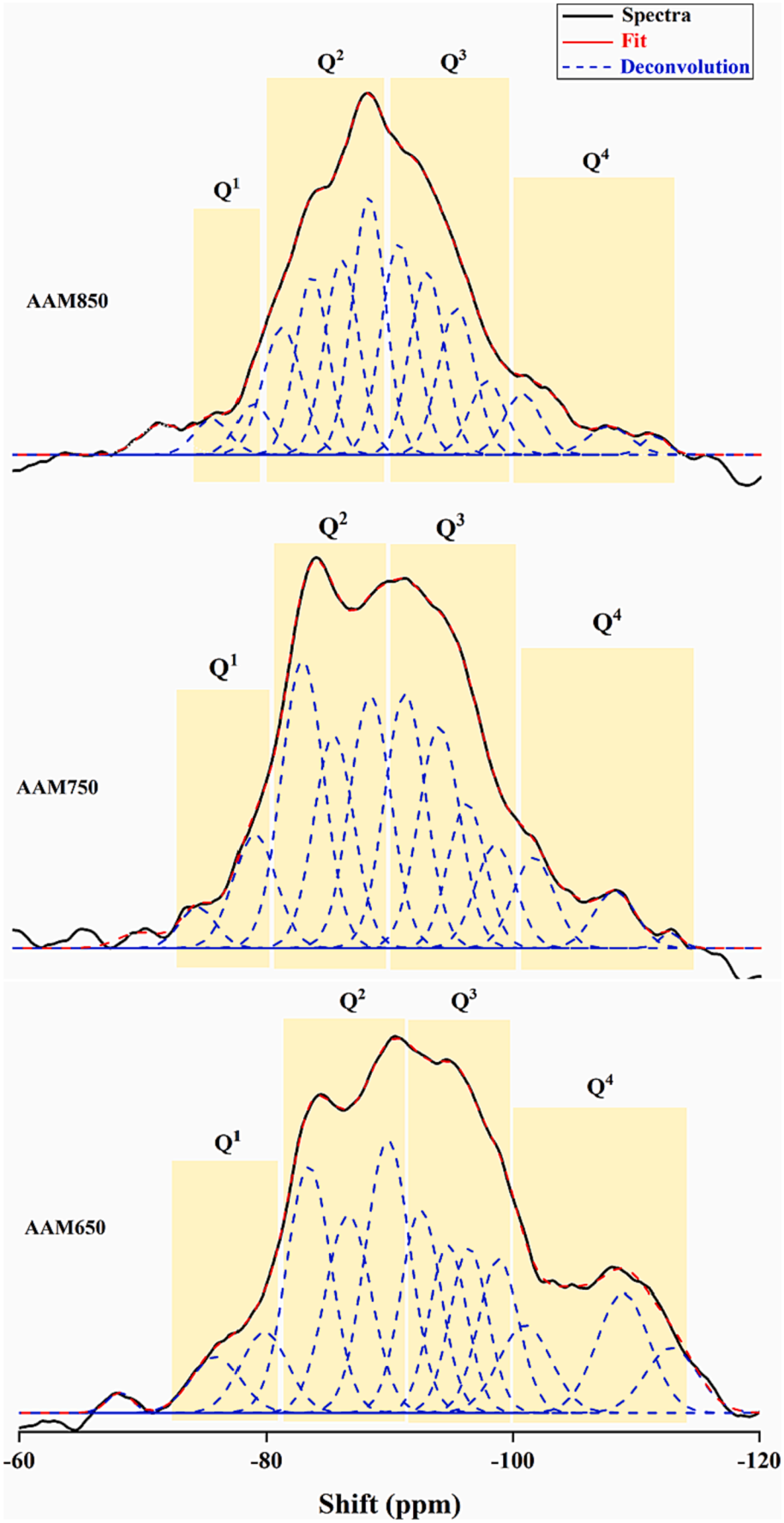

Fig. 11. Deconvoluted ^{29}Si NMR spectra of AAM650, AAM750, and AAM850.

Table 3
Deconvolution results of ^{29}Si MAS NMR of elaborated AAMs.

	AAM650		AAM750		AAM850	
	Center (ppm)	Area (%)	Center (ppm)	Area (%)	Center (ppm)	Area (%)
Q^0	71,89	2,19	70,2	0,88	68,16	6,18
Q^1	77,96	4,16	77,84	2,87	77,91	6,22
Q^1	79,30	8,20	79,38	6,46	79,83	7,47
Q^2(1Al)	83,95	14,66	83,19	17,35	83,43	12,85
Q^2	86,33	11,59	85,68	11,01	86,62	10,69
Q^3(1Al)	88,50	14,92	88,61	13,88	89,84	14,27
Q^3	91,90	9,57	91,43	13,38	92,52	10,95
Q^3	93,17	7,37	94,17	12,32	94,74	9,07
Q^3	95,56	7,31	96,37	7,30	96,43	7,29
Q^4(2Al)	98,02	7,69	98,67	5,57	98,83	7,26
Q^4(1Al)	100,85	5,94	101,74	5,00	100,99	5,42
Q^4	107,79	8,58	108,24	4,85	108,96	8,32

results could explain the highest strength that reached 38 MPa for AAM750 confirming the contribution of M—S—H in the development of mechanical properties.

Fig. 12 shows the SEM images of AAM after 120 days of curing. As shown in the figure, AAMs made from marls calcined at 750 °C and 850 °C reveal a relatively dense and uniform matrix microstructure with the presence of some pores and unreacted particles. The pore sizes are different for AAM750 and AAM850, with the latter one having smaller pores. However, the calcination temperature of 650 °C leads to a porous microstructure after the alkali activation reaction.

The EDX analysis of elaborated AAMs in Fig. 12showed the presence of the same dominant peaks of Si, Ca, Na and Mg, with the presence of low amount of Al. For AAM650 the major peaks were Si and Na with low amount of Mg and Al. This fact could be explained by the presence of silica gel and crystals of unreacted periclase. In addition, EDS of AAM750 confirmed the existence of both M—S—H and C—S—H gels

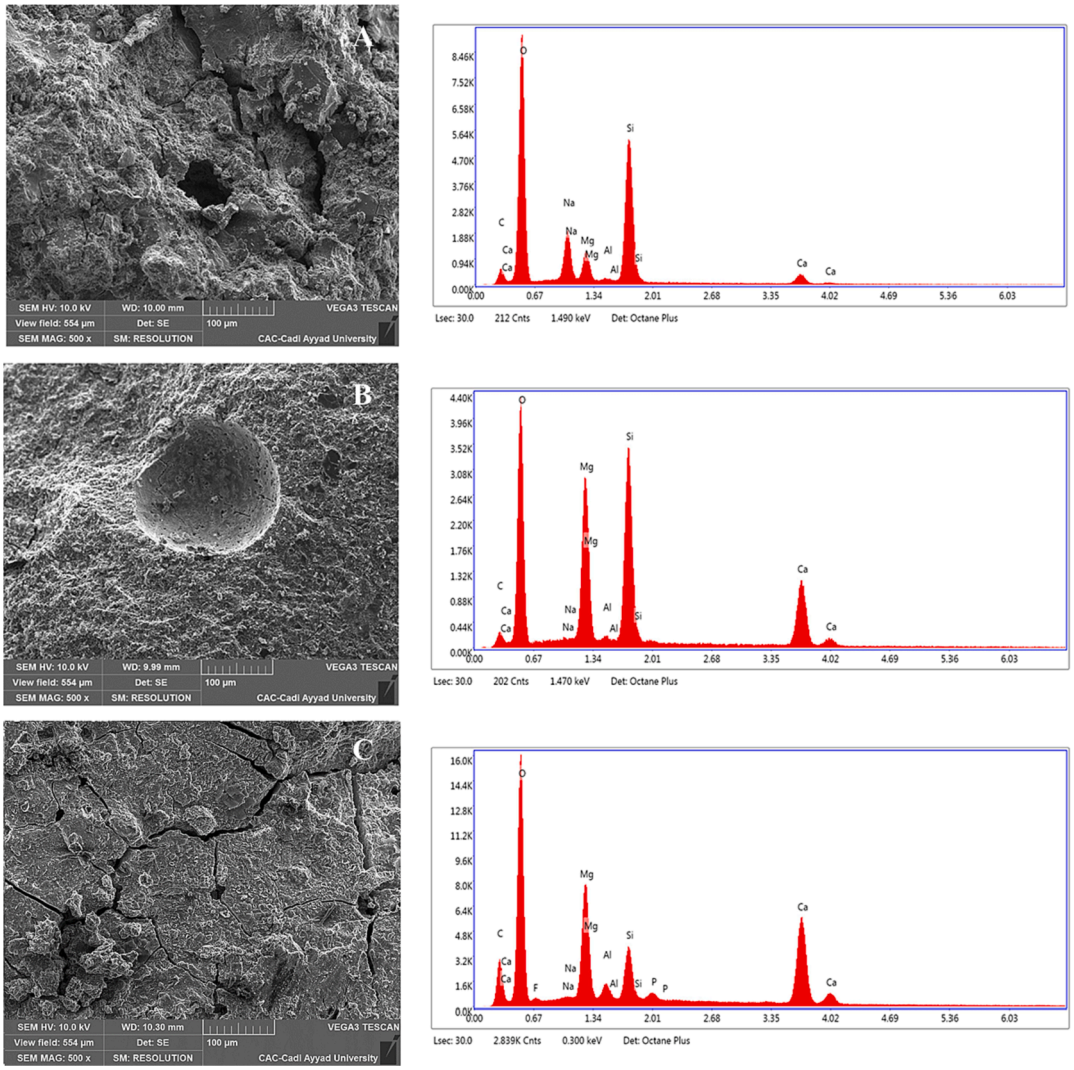

Fig. 12. SEM/EDX analysis of elaborated geopolymers microstructure after 120 days of curing. A: AAM650, B: AAM750, and C: AAM850.

with low amount of Al. However, AAM850 showed the co-precipitation of the same gels with high amount of Mg referring to the presence of unreacted periclase.

These results indicated the probable formation of a mixture of C—S—H and M—S—H gels. With the low Al content, there is the possibility of forming a hybrid gel containing Ca and Na (C-(N)-A—S—H) [80].

4. Conclusion

Sedimentary phosphate mines generate huge volume of waste rocks consisting of marls rocks that could be used as precursor for AAMs production. Several parameters affect deeply the mechanical strength including the calcination regime that was studied in the present work. However, an optimization of other experimental parameters could lead to interesting properties.

This work provides the findings below:

- RM consists of palygorskite phase as a clayey mineral that reached the total dihydroxylation at 750 °C.
- The dissolution of Al and Si was at the maximum for a temperature of T = 850 °C and in NaOH of 10 M. The increase of the concentration leads to the increase in coagulation of silica gels resulting in the decrease of dissolved Si ions. While the aluminum dissolution remains low due to the low percentage of Al_2O_3 in the raw marl.
- Hardened materials revealed that the AAM made of marl calcined at 750 °C presents the maximum UCS of about 38 MPa after 120 days of curing, while it decreased at 850 °C.
- The SEM/EDX and ^{29}Si - ^{27}Al MAS NMR analyses confirm the probable formation of C—S—H gel as the main reaction product with the existence of (C,N)-A—S—H gel. The MgO content in marls is subsequently high leading to the formation of M—S—H. [46]

CRediT authorship contribution statement

S. Mabroum: Conceptualization, Methodology, Formal analysis, Writing – original draft. **I. Garcia-Lodeiro:** Investigation, Writing – original draft, Writing – review & editing. **M.T. Blanco-Varela:** Investigation, Writing – original draft, Writing – review & editing. **Y. Taha:** Investigation, Writing – original draft, Writing – review & editing. **S. Chhaiba:** Formal analysis, Writing – review & editing. **S. Indris:** Formal analysis, Writing – review & editing. **M. Benzaazoua:** Supervision, Methodology, Writing – review & editing. **M. Mansori:** Conceptualization, Validation, Writing – original draft. **R. Hakkou:** Supervision, Methodology, Writing – review & editing.

Declaration of Competing Interest

The authors declare that they have no known competing financial interests or personal relationships that could have appeared to influence the work reported in this paper.

Data availability

No data was used for the research described in the article.

Acknowledgements

The authors are acknowledged the concession of the project ICOOP + 2020 (ref COOPA20454) - (JIN Projects 2021 PID2020-116738RJ-I00)- funded by the CSIC.

This work was support by OCP-SA, Morocco, under the specific agreement OCP/UM6P #AS03.

References

[1] M.F. Alnahhal, A. Hamdan, A. Hajimohammadi, T. Kim, Effect of rice husk ash-derived activator on the structural build-up of alkali activated materials, Cem Concr Res. 150 (2021), 106590, https://doi.org/10.1016/J.CEMCONRES.2021.106590.

[2] Y. Kou, H. Jiang, L. Ren, E. Yilmaz, Y. Li, Rheological Properties of Cemented Paste Backfill with Alkali-Activated Slag, Minerals 2020, Vol. 10, Page 288. 10 (2020) 288. 10.3390/MIN10030288.

[3] A. Palomo, J.I. López de la Fuente, Alkali-activated cementitous materials: Alternative matrices for the immobilisation of hazardous wastes: Part I, Stabilisation of boron, Cem Concr Res. 33 (2003) 281–288, https://doi.org/10.1016/S0008-8846(02)00963-8.

[4] J.G.S. van Jaarsveld, G.C. Lukey, J.S.J. van Deventer, A. Graham, The Stabilisation of Mine Tailings by Reactive Geopolymerisation, n.d.

[5] X. Dai, L. Ren, X. Gu, E. Yilmaz, K. Fang, H. Jiang, Strength Analysis and Optimization of Alkali Activated Slag Backfills Through Response Surface Methodology, Front Mater. 9 (2022) 96, https://doi.org/10.3389/FMATS.2022.844608/BIBTEX.

[6] B. Ren, Y. Zhao, H. Bai, S. Kang, T. Zhang, S. Song, Eco-friendly geopolymer prepared from solid wastes: A critical review, Chemosphere 267 (2021), 128900, https://doi.org/10.1016/j.chemosphere.2020.128900.

[7] X. Tian, W. Xu, S. Song, F. Rao, L. Xia, Effects of curing temperature on the compressive strength and microstructure of copper tailing-based geopolymers, Chemosphere 253 (2020), 126754, https://doi.org/10.1016/j.chemosphere.2020.126754.

[8] G. Xue, E. Yilmaz, Strength, acoustic, and fractal behavior of fiber reinforced cemented tailings backfill subjected to triaxial compression loads, Constr Build Mater. 338 (2022), 127667, https://doi.org/10.1016/J.CONBUILDMAT.2022.127667.

[9] L. Mancini, S. Sala, Social impact assessment in the mining sector: Review and comparison of indicators frameworks, Resour. Policy 57 (2018) 98–111, https://doi.org/10.1016/j.resourpol.2018.02.002.

[10] P. Blanc, A. Lach, A. Lassin, M. Falah, R. Obenaus-Emler, S. Guignot, Modeling hydration of mine tailings: Production of hydraulic binders from alkali-activated materials, Cem Concr Res. 137 (2020), 106216, https://doi.org/10.1016/J.CEMCONRES.2020.106216.

[11] J. Wu, J. Li, F. Rao, W. Yin, Mechanical property and structural evolution of alkali-activated slag-phosphate mine tailings mortars, Chemosphere 251 (2020), 126367, https://doi.org/10.1016/j.chemosphere.2020.126367.

[12] K.A. Hudson-Edwards, B. Dold, Mine Waste Characterization, Management and Remediation, Minerals 2015, Vol. 5, Pages 82-85. 5 (2015) 82–85. 10.3390/MIN5010082.

[13] Z. Bian, X. Miao, S. Lei, S. Chen, W. Wang, S. %J S. Struthers, The challenges of reusing mining and mineral-processing wastes, 337 (2012) 702–703.

[14] I. Park, C.B. Tabelin, S. Jeon, X. Li, K. Seno, M. Ito, N. Hiroyoshi, A review of recent strategies for acid mine drainage prevention and mine tailings recycling, Chemosphere 219 (2019) 588–606, https://doi.org/10.1016/j.chemosphere.2018.11.053.

[15] Y. Taha, M. Benzaazoua, R. Hakkou, M. Mansori, Coal mine wastes recycling for coal recovery and eco-friendly bricks production, Miner Eng. 107 (2017) 123–138, https://doi.org/10.1016/j.mineng.2016.09.001.

[16] Y. Taha, M. Benzaazoua, M. Edahbi, M. Mansori, R. Hakkou, Leaching and geochemical behavior of fired bricks containing coal wastes, J Environ Manage. 209 (2018) 227–235, https://doi.org/10.1016/J.JENVMAN.2017.12.060.

[17] A. El Machi, S. Mabroum, Y. Taha, A. Tagnit-Hamou, M. Benzaazoua, R. Hakkou, Use of flint from phosphate mine waste rocks as an alternative aggregates for concrete, Constr Build Mater. 271 (2021), 121886, https://doi.org/10.1016/j.conbuildmat.2020.121886.

[18] A. El Machi, S. Mabroum, Y. Taha, A. Tagnit-Hamou, M. Benzaazoua, R. Hakkou, Valorization of phosphate mine waste rocks as aggregates for concrete, Mater Today Proc. (2020), https://doi.org/10.1016/j.matpr.2020.08.404.

[19] M. Loutou, M. Hajjaji, M. Mansori, C. Favotto, R. Hakkou, Phosphate sludge: Thermal transformation and use as lightweight aggregate material, J Environ Manage. 130 (2013) 354–360, https://doi.org/10.1016/j.jenvman.2013.09.004.

[20] A. Bahhou, Y. Taha, Y. El Khessaimi, H. Idrissi, R. Hakkou, J. Amalik, M. Benzaazoua, Use of phosphate mine by-products as supplementary cementitious materials, Mater Today Proc, Elsevier Ltd, in, 2020, pp. 3781–3788.

[21] A. Bahhou, Y. Taha, Y. El Khessaimi, R. Hakkou, A. Tagnit-Hamou, M. Benzaazoua, Using calcined marls as non-common supplementary cementitious materials—a critical review, Minerals. 11 (2021) 517, https://doi.org/10.3390/min11050517.

[22] N.T. Dung, C. Unluer, Improving the performance of reactive MgO cement-based concrete mixes, Constr Build Mater. 126 (2016) 747–758, https://doi.org/10.1016/J.CONBUILDMAT.2016.09.090.

[23] M. Liska, A. Al-Tabbaa, Performance of magnesia cements in pressed masonry units with natural aggregates: Production parameters optimisation, Constr Build Mater. 22 (2008) 1789–1797, https://doi.org/10.1016/J.CONBUILDMAT.2007.05.007.

[24] H.M. Tran, A. Scott, Strength and workability of magnesium silicate hydrate binder systems, Constr Build Mater. 131 (2017) 526–535, https://doi.org/10.1016/J.CONBUILDMAT.2016.11.109.

[25] E. Bernard, B. Lothenbach, F. Le Goff, I. Pochard, A. Dauzères, Effect of magnesium on calcium silicate hydrate (C-S-H), Cem Concr Res. 97 (2017) 61–72, https://doi.org/10.1016/J.CEMCONRES.2017.03.012.

[26] A.M. Humad, K. Habermehl-Cwirzen, A. Cwirzen, Effects of Fineness and Chemical Composition of Blast Furnace Slag on Properties of Alkali-Activated Binder, Materials 2019, Vol. 12, Page 3447. 12 (2019) 3447. 10.3390/MA12203447.

[27] M. Ben Haha, B. Lothenbach, G. Le Saout, F. Winnefeld, Influence of slag chemistry on the hydration of alkali-activated blast-furnace slag — Part I: Effect of MgO, Cem Concr Res. 41 (2011) 955–963, https://doi.org/10.1016/J.CEMCONRES.2011.05.002.

[28] F. Jin, K. Gu, A. Al-Tabbaa, Strength and drying shrinkage of reactive MgO modified alkali-activated slag paste, Constr Build Mater. 51 (2014) 395–404, https://doi.org/10.1016/J.CONBUILDMAT.2013.10.081.

[29] B. Lothenbach, D. Nied, E. L'Hôpital, G. Achiedo, A. Dauzères, Magnesium and calcium silicate hydrates, Cem Concr Res. 77 (2015) 60–68, https://doi.org/10.1016/J.CEMCONRES.2015.06.007.

[30] S. Mabroum, S. Moukannaa, A. El Machi, Y. Taha, M. Benzaazoua, R. Hakkou, Mine wastes based geopolymers: A critical review, Clean, Eng Technol. (2020), 100014, https://doi.org/10.1016/j.clet.2020.100014.

[31] N. Ouffa, M. Benzaazoua, T. Belem, R. Trauchessec, A. Lecomte, Alkaline dissolution potential of aluminosilicate minerals for the geosynthesis of mine paste backfill, Mater Today Commun. 24 (2020), 101221, https://doi.org/10.1016/j.mtcomm.2020.101221.

[32] L.Y. Zhang, S. Ahmari, J.H. Zhang, Synthesis and characterization of fly ash modified mine tailings-based geopolymers, Constr Build Mater. 25 (2011) 3773–3781, https://doi.org/10.1016/j.conbuildmat.2011.04.005.

[33] X. Jiao, Y. Zhang, T. Chen, S. Bao, T. Liu, J. Huang, Geopolymerisation of a silica-rich tailing, Miner Eng. 24 (2011) 1710–1712, https://doi.org/10.1016/j.mineng.2011.09.008.

[34] N. Ye, J. Yang, X. Ke, J. Zhu, Y. Li, C. Xiang, H. Wang, L. Li, B.o. Xiao, J. Biernacki, Synthesis and characterization of geopolymer from bayer red mud with thermal pretreatment, J. Am. Ceram. Soc. 97 (5) (2014) 1652–1660.

[35] T. Hertel, B. Blanpain, Y. Pontikes, A Proposal for a 100 % Use of Bauxite Residue Towards Inorganic Polymer Mortar, Journal of Sustainable Metallurgy. 2 (2016) 394–404, https://doi.org/10.1007/s40831-016-0080-6.

[36] S. Mabroum, A. Aboulayt, Y. Taha, M. Benzaazoua, N. Semlal, R. Hakkou, Elaboration of geopolymers based on clays by-products from phosphate mines for construction applications, J Clean Prod. 261 (2020), 121317, https://doi.org/10.1016/j.jclepro.2020.121317.

[37] S. Mabroum, Y. Taha, M. Benzaazoua, R. Hakkou, Recycling of marls from phosphate by-products to produce alkali-activated geopolymers, Mater Today Proc. (2021), https://doi.org/10.1016/j.matpr.2021.03.206.

[38] J.L. Provis, Alkali-Activation of Calcined Clays – Past, Present and Future, RILEM Bookseries. 16 (2018) 372–376, https://doi.org/10.1007/978-94-024-1207-9_60.

[39] T. Danner, G. Norden, H. Justnes, Calcareous smectite clay as a pozzolanic alternative to kaolin, Eur. J. Environ. Civ. Eng. (2019), https://doi.org/10.1080/19648189.2019.1590741.

[40] N.R. Rakhimova, R.Z. Rakhimov, V.P. Morozov, A.R. Gaifullin, L.I. Potapova, A. M. Gubaidullina, Y.N. Osin, Marl-based geopolymers incorporated with limestone: A feasibility study, J Non Cryst Solids. 492 (2018) 1–10, https://doi.org/10.1016/j.jnoncrysol.2018.04.015.

[41] H. Xu, J.S.J. Van Deventer, The geopolymerisation of alumino-silicate minerals, Int J Miner Process. 59 (2000) 247–266, https://doi.org/10.1016/S0301-7516(99)00074-5.

[42] V. Poussardin, M. Paris, A. Tagnit-Hamou, D. Deneele, Potential for calcination of a palygorskite-bearing argillaceous carbonate, Appl Clay Sci. 198 (2020), 105846, https://doi.org/10.1016/j.clay.2020.105846.

[43] F. Gan, J. Zhou, H. Wang, C. Du, X. Chen, Removal of phosphate from aqueous solution by thermally treated natural palygorskite, Water Res. 43 (2009) 2907–2915, https://doi.org/10.1016/j.watres.2009.03.051.

[44] J.J. Xie, T. Chen, B. Xing, H. Liu, Q. Xie, H. Li, Y. Wu, The thermochemical activity of dolomite occurred in dolomite-palygorskite, Appl Clay Sci. 119 (2016) 42–48, https://doi.org/10.1016/j.clay.2015.07.014.

[45] M. Loutou, Y. Taha, M. Benzaazoua, Y. Daafi, R. Hakkou, Valorization of clay by-product from moroccan phosphate mines for the production of fired bricks, J Clean Prod. 229 (2019) 169–179, https://doi.org/10.1016/j.jclepro.2019.05.003.

[46] *,† M. Halmann, ‡ and A. Frei, § A. Steinfeld‡, Magnesium Production by the Pidgeon Process Involving Dolomite Calcination and MgO Silicothermic Reduction: Thermodynamic and Environmental Analyses, (2008). 10.1021/IE071234V.

[48] F. Bullerjahn, M. Zajac, J. Pekarkova, D. Nied, Novel SCM produced by the co-calcination of aluminosilicates with dolomite, Cem Concr Res. 134 (2020), 106083, https://doi.org/10.1016/J.CEMCONRES.2020.106083.

[49] B. Yoosuk, P. Udomsap, B. Puttasawat, P. Krasae, Modification of calcite by hydration-dehydration method for heterogeneous biodiesel production process: The effects of water on properties and activity, Chem. Eng. J. 162 (2010) 135–141, https://doi.org/10.1016/j.cej.2010.05.013.

[50] H. Cheng, R.L. Frost, J. Yang, Q. Liu, J. He, Infrared and infrared emission spectroscopic study of typical Chinese kaolinite and halloysite, Spectrochim Acta A Mol Biomol Spectrosc. 77 (2010) 1014–1020, https://doi.org/10.1016/j.saa.2010.08.039.

[51] J. Zhu, P. Zhang, Y. Wang, K. Wen, X. Su, R. Zhu, H. He, Y. Xi, Effect of acid activation of palygorskite on their toluene adsorption behaviors, Appl Clay Sci. 159 (2018) 60–67, https://doi.org/10.1016/J.CLAY.2017.07.019.

[52] G. Besson, Refined Relationships between Chemical Composition of Dioctahedral Fine-Grained Mica Minerals and Their Infrared Spectra within the OH Stretching Region. Part I: Identification of the OH Stretching Bands, Clay Clay Miner. 45 (2) (1997) 158–169.

[53] R. Rusmin, B. Sarkar, B. Biswas, J. Churchman, Y. Liu, R. Naidu, Structural, electrokinetic and surface properties of activated palygorskite for environmental application, Appl Clay Sci. 134 (2016) 95–102, https://doi.org/10.1016/j.clay.2016.07.012.

[54] V. Poussardin, M. Paris, W. Wilson, A. Tagnit-Hamou, D. Deneele, Self-reactivity of a calcined palygorskite-bearing marlstone for potential use as supplementary cementitious material, Appl Clay Sci. 216 (2022), 106372, https://doi.org/10.1016/J.CLAY.2021.106372.

[55] G. Rim, A.K. Marchese, P. Stallworth, S.G. Greenbaum, A.H.A. Park, 29Si solid state MAS NMR study on leaching behaviors and chemical stability of different Mg-silicate structures for CO2 sequestration, Chem. Eng. J. 396 (2020), 125204, https://doi.org/10.1016/J.CEJ.2020.125204.

[56] R. Dabbebi, J.L.B. de Aguiar, B. Samet, S. Baklouti, Mineralogical and chemical investigation of Tunisian phosphate washing waste during calcination, J Therm Anal Calorim. 137 (2019) 1827–1840, https://doi.org/10.1007/S10973-019-08057-3/TABLES/4.

[57] R. Oestrike, W.-H. Yang, R.J. Kirkpatrick, R.L. Hervig, A. Navrotsky, B. Montez, High-resolution 23Na, 27Al and 29Si NMR spectroscopy of framework Aluminosilicate glasses, Geochim. Cosmochim. Acta 51 (8) (1987) 2199–2209.

[58] U. Rattanasak, P. Chindaprasirt, Influence of NaOH solution on the synthesis of fly ash geopolymer, Miner Eng. 22 (2009) 1073–1078, https://doi.org/10.1016/j.mineng.2009.03.022.

[59] D. Bondar, C.J. Lynsdale, N.B. Milestone, N. Hassani, A.A. Ramezanianpour, Effect of type, form, and dosage of activators on strength of alkali-activated natural pozzolans, Cem Concr Compos. 33 (2011) 251–260, https://doi.org/10.1016/J.CEMCONCOMP.2010.10.021.

[60] V.F.F. Barbosa, K.J.D. MacKenzie, C. Thaumaturgo, Synthesis and characterisation of materials based on inorganic polymers of alumina and silica: sodium polysialate polymers, Int. J. Inorg. Mater. 2 (2000) 309–317, https://doi.org/10.1016/S1466-6049(00)00041-6.

[61] M.J. Sánchez-Herrero, A. Fernández-Jiménez, Á. Palomo, L. Klein, Alkaline Hydration Of C2S and C3S, J. Am. Ceram. Soc. 99 (2016) 604–611, https://doi.org/10.1111/JACE.13985.

[62] J. Temuujin, A. van Riessen, R. Williams, Influence of calcium compounds on the mechanical properties of fly ash geopolymer pastes, J Hazard Mater. 167 (2009) 82–88, https://doi.org/10.1016/J.JHAZMAT.2008.12.121.

[63] Q. Wan, F. Rao, S. Song, Reexamining calcination of kaolinite for the synthesis of metakaolin geopolymers - roles of dehydroxylation and recrystallization, J Non Cryst Solids. 460 (2017) 74–80, https://doi.org/10.1016/J.JNONCRYSOL.2017.01.024.

[64] A. Elimbi, H.K. Tchakoute, D. Njopwouo, Effects of calcination temperature of kaolinite clays on the properties of geopolymer cements, Constr Build Mater. 25 (2011) 2805–2812, https://doi.org/10.1016/J.CONBUILDMAT.2010.12.055.

[65] R. Firdous, D. Stephan, Effect of silica modulus on the geopolymerization activity of natural pozzolans, Constr Build Mater. 219 (2019) 31–43, https://doi.org/10.1016/J.CONBUILDMAT.2019.05.161.

[66] H. Jiang, J. Han, Y. Li, E. Yilmaz, Q. Sun, J. Liu, Relationship between ultrasonic pulse velocity and uniaxial compressive strength for cemented paste backfill with alkali-activated slag, 10.1080/10589759.2019.1679140. 35 (2019) 359–377. 10.1080/10589759.2019.1679140.

[67] D. Nied, K. Enemark-Rasmussen, E. L'Hopital, J. Skibsted, B. Lothenbach, Properties of magnesium silicate hydrates (M-S-H), Cem Concr Res. 79 (2016) 323–332, https://doi.org/10.1016/J.CEMCONRES.2015.10.003.

[68] H.A. Abdel-Gawwad, S. Abd El-Aleem, A.A. Amer, H. El-Didamony, M.A. Arif, Combined impact of silicate-amorphicity and MgO-reactivity on the performance of Mg-silicate cement, Constr Build Mater. 189 (2018) 78–85, https://doi.org/10.1016/J.CONBUILDMAT.2018.08.171.

[69] T. Zhang, J. Zou, B. Wang, Z. Wu, Y. Jia, C.R. Cheeseman, Characterization of Magnesium Silicate Hydrate (MSH) Gel Formed by Reacting MgO and Silica Fume, Materials 2018, Vol. 11, Page 909. 11 (2018) 909. 10.3390/MA11060909.

[70] D. Panias, I.P. Giannopoulou, T. Perraki, Effect of synthesis parameters on the mechanical properties of fly ash-based geopolymers, Colloids Surf A Physicochem Eng Asp. 301 (2007) 246–254, https://doi.org/10.1016/J.COLSURFA.2006.12.064.

[71] K. Boonserm, V. Sata, K. Pimraksa, P. Chindaprasirt, Improved geopolymerization of bottom ash by incorporating fly ash and using waste gypsum as additive, Cem Concr Compos. 34 (2012) 819–824, https://doi.org/10.1016/J.CEMCONCOMP.2012.04.001.

[72] S. Hanjitsuwan, B. Injorhor, T. Phoo-ngernkham, N. Damrongwiriyanupap, L.Y. Li, P. Sukontasukkul, P. Chindaprasirt, Drying shrinkage, strength and microstructure of alkali-activated high-calcium fly ash using FGD-gypsum and dolomite as expansive additive, Cem Concr Compos. 114 (2020), 103760, https://doi.org/10.1016/J.CEMCONCOMP.2020.103760.

[73] H.A. Abdel-Gawwad, S. Abd El-Aleem, Effect of reactive magnesium oxide on properties of alkali activated slag geopolymer cement pastes, Ceramics-Silikáty 59 (2015) 37–47.

[74] E. Bernard, B. Lothenbach, D. Rentsch, I. Pochard, A. Dauzères, Formation of magnesium silicate hydrates (M-S-H), Physics and Chemistry of the Earth, Parts A/B/C. 99 (2017) 142–157, https://doi.org/10.1016/J.PCE.2017.02.005.

[75] E. Bernard, B. Lothenbach, C. Cau-Dit-Coumes, C. Chlique, A. Dauzères, I. Pochard, Magnesium and calcium silicate hydrates, Part I: Investigation of the possible magnesium incorporation in calcium silicate hydrate (C-S-H) and of the calcium in magnesium silicate hydrate (M-S-H), Appl. Geochem. 89 (2018) 229–242, https://doi.org/10.1016/J.APGEOCHEM.2017.12.005.

[76] F. Jin, A. Al-Tabbaa, Thermogravimetric study on the hydration of reactive magnesia and silica mixture at room temperature, Thermochim Acta. 566 (2013) 162–168, https://doi.org/10.1016/J.TCA.2013.05.036.

[77] E. Bernard, B. Lothenbach, C. Chlique, M. Wyrzykowski, A. Dauzères, I. Pochard, C. Cau-Dit-Coumes, Characterization of magnesium silicate hydrate (M-S-H), Cem

Concr Res. 116 (2019) 309–330, https://doi.org/10.1016/J.CEMCONRES.2018.09.007.
[78] L. Fernandez, C. Alonso, C. Andrade, A. Hidalgo, The interaction of magnesium in hydration of C3S and CSH formation using 29Si MAS-NMR, J Mater Sci. 43 (2008) 5772–5783, https://doi.org/10.1007/S10853-008-2889-2/FIGURES/7.
[79] T. Bräuniger, M. Jansen, Solid-state NMR spectroscopy of quadrupolar nuclei in inorganic chemistry, Z Anorg Allg Chem. 639 (2013) 857–879, https://doi.org/10.1002/zaac.201300102.
[80] E. Bernard, B. Lothenbach, C. Cau-Dit-Coumes, I. Pochard, D. Rentsch, Aluminum incorporation into magnesium silicate hydrate (M-S-H), Cem Concr Res. 128 (2020), 105931, https://doi.org/10.1016/J.CEMCONRES.2019.105931.
[81] E. Bernard, B. Lothenbach, I. Pochard, C. Cau-Dit-Coumes, Alkali binding by magnesium silicate hydrates, J. Am. Ceram. Soc. 102 (2019) 6322–6336, https://doi.org/10.1111/JACE.16494.
[82] S.A. Bernal, J.L. Provis, B. Walkley, R. San Nicolas, J.D. Gehman, D.G. Brice, A. R. Kilcullen, P. Duxson, J.S.J. Van Deventer, Gel nanostructure in alkali-activated binders based on slag and fly ash, and effects of accelerated carbonation, Cem Concr Res. 53 (2013) 127–144, https://doi.org/10.1016/J.CEMCONRES.2013.06.007.
[83] A.M. Moreno de los Reyes, J.A. Suárez-Navarro, M.D.M. Alonso, C. Gascó, I. Sobrados, F. Puertas, Hybrid Cements: Mechanical Properties, Microstructure and Radiological Behavior., Molecules. 27 (2022). 10.3390/MOLECULES27020498.
[84] C.A. Fyfe, H. Gies, Y. Feng, Three-Dimensional Lattice Connectivities from Two-Dimensional High-Resolution Solid-State NMR. 29Si MAS NMR Investigation of the Silicate Lattice of Zeolite ZSM-39 (Dodecasil 3C), J Am Chem Soc. 111 (1989) 7702–7707. 10.1021/JA00202A006.